Journal of
Materials Chemistry A

PAPER

View Article Online
View Journal | View Issue

Check for updates

Cite this: *J. Mater. Chem. A*, 2020, **8**, 11282

Cu/M:ZnO (M = Mg, Al, Cu) colloidal nanocatalysts for the solution hydrogenation of carbon dioxide to methanol†

Alice H. M. Leung,[a] Andrés García-Trenco,[a] Andreas Phanopoulos,[a] Anna Regoutz,[b] Manfred E. Schuster,[c] Sebastian D. Pike,[a] Milo S. P. Shaffer*[de] and Charlotte K. Williams*[a]

Received 13th January 2020
Accepted 15th May 2020

DOI: 10.1039/d0ta00509f

rsc.li/materials-a

Doped-ZnO nanoparticles, capped with dioctylphosphinate ligands, are synthesised by the controlled hydrolysis of a mixture of organometallic precursors. Substitutional doping of the wurtzite ZnO nanoparticles with 5 mol% Mg(II), Al(III) and Cu(I) is achieved by the addition of sub-stoichiometric amounts of the appropriate dopant [(*n*-butyl)(*sec*-butyl)magnesium, triethylaluminium or mesitylcopper] to diethylzinc in the precursor mixture. After hydrolysis, the resulting colloidal nanoparticles (sizes of 2–3 nm) are characterised by powder X-ray crystallography, transmission electron microscopy, inductively-coupled plasma optical emission spectrometry and X-ray photoelectron spectroscopy. A solution of the doped-ZnO nanoparticles and colloidal Cu(0) nanoparticles [M:ZnO : Cu = 1 : 1] are applied as catalysts for the hydrogenation of CO_2 to methanol in a liquid-phase continuous flow stirred tank reactor [210 °C, 50 bar, $CO_2 : H_2 = 1 : 3$, 150 mL min^{-1}, mesitylene, 20 h]. All the catalyst systems display higher rates of methanol production and better stability than a benchmark heterogeneous catalyst, Cu–ZnO–Al_2O_3 [480 μmol mmol$_{metal}^{-1}$ h^{-1}], with approximately twice the activity for the Al(III)-doped nanocatalyst. Despite outperforming the benchmark catalyst, Mg(II) doping is detrimental towards methanol production in comparison to undoped ZnO. X-Ray photoelectron spectroscopy and transmission electron microscopy analysis of the most active post-catalysis samples implicate the migration of Al(III) to the catalyst surface, and this surface enrichment is proposed to facilitate stabilisation of the catalytic ZnO/Cu interfaces.

Introduction

The doping of semiconductors is critical for manipulating carrier density and band-gap in (opto)electronics, and in catalysis to control activity, selectivity and lifetime.[1,2] Zinc oxide, a wide band-gap (3.3 eV), n-type semiconductor, is an important material in both contexts, providing useful properties such as transparency and accessible redox chemistry, while using only abundant elements.[3–7] Consequently, ZnO nanoparticles (NPs) have found use as solution-processible electronic inks, and as high surface area catalysts.[8–10] Relevant to this work are elegant examples of property enhancement through heterovalent substitutional doping of ZnO.[3,11–14] Depending on the dopant either shallow energy level donor (n-type) or acceptor (p-type) states are incorporated, adjusting the properties.[3] To synthesise these materials, a judicious choice of reactants and conditions must be employed to balance the reactivity of the host and dopant *i.e.* to prevent phase separation.[1,4] n-Type ZnO doping is more easily achieved and is most often accomplished through incorporation of Group 13 elements at interstitial sites.[3] For instance, aluminium doping enhanced the optical and electronic properties of ZnO, affording a cheaper and less toxic competitor to the ubiquitous transparent conducting oxide, indium tin oxide (ITO).[11] Alternatively, doping with Mg(II) afforded colloidal solutions that were better reductants than ZnO, as demonstrated by the rapid and spontaneous electron transfer from $Zn_{0.75}Mg_{0.25}O$ to ZnO.[14] On the other hand, p-type doping often suffers from compensating mechanisms during synthesis, such as the presence of low-energy native defects (interstitial zinc atoms or oxygen vacancies) or background impurities.[3] Nevertheless, ZnO doping with Group 1 elements[15]

---

[a] *Chemistry Research Laboratory, University of Oxford, 12 Mansfield Road, Oxford, OX1 3TA, UK. E-mail: charlotte.williams@chem.ox.ac.uk*

[b] *Department of Chemistry, University College London, 20 Gordon Street, London WC1H 0AJ, UK*

[c] *Johnson Matthey Technology Centre, Blount's Court, Sonning Common, RG4 9NH, UK*

[d] *Department of Chemistry, Imperial College London, London, SW7 2AZ, UK. E-mail: m.shaffer@imperial.ac.uk*

[e] *Department of Materials, Imperial College London, London, SW7 2AZ, UK*

† Electronic supplementary information (ESI) available: Tables outlining amount of dopant precursor used and mass analysis by EA and TGA. Additional figures showing nanocatalyst characterisation, methanol production rates and selectivity as well as post-catalysts characterisation. Rationale for catalytic reaction conditions used. See DOI: 10.1039/d0ta00509f

or Cu(I)[16] has been achieved. For instance, the thermal treatment of heterometallic cubane ([$Me_3Zn_3M(THF)O^tBu_4$], M = Li, Na, K), at 750 °C for 3 h, produced p-type ZnO nanoparticles (20–70 nm) with dopant levels up to 10 mol%.[15,17] Ultimately, the successful and reproducible, large-scale fabrication of both n- and p-type doped-ZnO could allow for production of ZnO p–n junctions for use in thin film, large area, potential transparent semiconducting electronic devices.[18–20]

Beyond semiconducting applications, ZnO is also one component of the industrial heterogeneous three-component catalyst Cu–ZnO–Al_2O_3, which is used to produce methanol on a 50 million-tonne scale in conjunction with a syn-gas feedstock.[21,22] Methanol is a clean burning liquid fuel that can be blended with petrol providing an attractive 'drop-in' substitute with existing fuels, and moreover can be generated from renewable raw materials (*i.e.* CO_2/H_2).[23–26] Doping the ZnO component can enhance the catalytic performance using either syn-gas or CO_2/H_2 gas mixtures.[27–29] The range of dopants includes alkaline metals (*e.g.* Cs(I) or Mg(II)),[30] transition (*e.g.* Zr(II) or Mn(II)/(III))[27,31] or main group metals (*e.g.* Al(III) or Ga(III)).[32,33] These dopants are proposed to increase activity by acting as electronic and/or structural promoters, *i.e.* by altering the electronic structure through addition of energy levels to reduce activation energy, or by modifying the catalyst nanostructure to increase the number of active sites, respectively.[28,34] In particular, there is an enhancement in activity when n-type dopants, such as Al(III) and Ga(III) are incorporated into Cu/ZnO catalysts.[28,29] It is proposed that dopants facilitate formation of Cu/ZnO interfaces by labilising the ZnO_x ($x < 1$) component.[35] These interfaces, often observed at step-defects in the Cu phase,[36] are the putative catalytic active sites.[29,37] Conversely, by lowering the density of donor states, *e.g.* by doping Cu/ZnO with Mg(II), an increase in optical band-gap and reduction potential were observed.[28] The lower efficiency for methanol production was attributed to the converse effects limiting the formation of critical Cu/ZnO_x interfaces.[28,29]

Most methanol production occurs using syn-gas in fixed bed reactor configurations but slurry phase methods, where the catalyst is suspended in solution, are attractive alternatives. This slurry process can improve reaction kinetics and may increase the intrinsic activity. As long as high enough pressures and dilute conditions are implemented, the mass transport effects can be managed, though for productivity reasons, reactors may, in fact, be operated near the mass transport limit.[38] Additionally, liquid phase synthesis may mitigate local hot spots, accelerate catalyst activation and facilitate continuous product removal. These benefits have led to the development of a commercial liquid-phase methanol synthesis process (LPMeOH™).[39] One method to optimize liquid phase processes is to develop colloidal (quasi-homogeneous) catalysts. Our group,[8,9,40–43] and others,[44–46] have previously outlined some of the advantages of such species including easy control over catalyst composition (Cu : Zn ratio), access to small, well-defined, high surface area nanoparticles, and control over surface chemistry. These colloidal catalysts have been applied either to the synthesis of methanol from syn-gas[21,47] or by carbon dioxide hydrogenation (CO_2/H_2).[9,40,41] They can show high activity and selectivity over the reverse water–gas shift (rWGS) reaction.[28]

To make these colloidal catalysts, we have developed a synthesis using the hydrolysis of organozinc reagents. The method generates small (2–4 nm) and monodispersed ZnO nanoparticles, which are soluble in a range of organic solvents.[48–50] The hydrolysis of organozinc compounds (*e.g.* $ZnPh_2$, $ZnCy_2$, $ZnEt_2$), in the presence of an aqueous stable, anionic coordinating ligand (*e.g.* carboxylate or phosphinate), readily generates soluble ZnO nanoparticles,[48,50–57] with a high density of surface defects, proposed to be beneficial for catalysis.[9,44,58] Hydrolytic syntheses provide straightforward control of ligand coverage and kinetic control over the growth of particles, allowing access to small ZnO nanoparticles (2–4 nm).[4,50,54,57] The methodology is potentially attractive for dopant incorporation since a second organometallic reagent can simply be added to the one-pot hydrolysis reaction. The synthesis of doped-ZnO nanoparticles *via* co-precipitation methods has allowed doping levels >10% (*e.g.* 18% Mg-,[14] 13% Al-[29] or 12% Cu-doping[59]) with a range of metals (*e.g.* Group 1,[15,17] Group 2,[14] Group 13,[28,29] and Group 11 [16,59–61]); however, there are only a few examples of successful doping using organometallic routes.[4,62,63] Chaudret and co-workers demonstrated that the addition of Li-amides during the hydrolysis of $ZnCy_2$, in the presence of octylamine, led to the formation of spherical Li-doped-ZnO nanoparticles (2.4–4.3 nm, Li content 1–10 mol%). The nanoparticle growth was controlled by the localisation of LiOH on the surface of ZnO.[62] Alternatively, our group prepared Mg-doped ZnO nanoparticles by mixing $ZnEt_2$ with $MgBu_2$ before hydrolysis, in the presence of dioctylphosphinic acid (DOPA–H, $(C_8H_{17})_2PO_2H$). The resultant particles showed up to 10% Mg incorporation into the wurtzite ZnO structure.[63]

This work aims to investigate the preparation of other doped ZnO materials, *e.g.* with Al(III), Mg(II) and Cu(I). These colloidal nanoparticles will be tested as components in liquid phase catalysts for the reduction of CO_2 to methanol.

Experimental

Materials and methods

The syntheses of all the ZnO nanoparticles were carried out in a dry nitrogen-filled glovebox and using Schlenk line techniques. All solvents were purchased from VWR, UK; all chemicals from Sigma Aldrich and were used as supplied, unless otherwise stated. Toluene was dried using an MBraun SPS-800 solvent purification system and degassed by sparging with N_2 for 1 h to remove oxygen. Diethyl zinc, triethyl aluminium and (*n*-butyl)(*sec*-butyl)magnesium are highly pyrophoric and volatile: extreme caution must be taken during usage. HPLC-grade water was used for the controlled hydrolysis experiments.

Elemental analyses were performed by Mr Stephen Boyer at London Metropolitan University and inductively-coupled plasma optical emission spectrometry (ICP-OES) was performed by Mr Alan Dickerson at the University of Cambridge.

Powder X-ray diffraction (XRD) experiments were performed using a PANalytical X'pert PRO diffractometer in the theta/theta reflection mode, fitted with a nickel filter, 0.04 rad Soller slit, 10 mm mask, 1/4° fixed divergence slit, and 1/2° fixed anti-scatter slit. An operating voltage of 40 kV was used with a step size of 0.033° 2θ, scan step time of 70 s and scan range of 10–80° 2θ. Air sensitive samples were prepared in a glovebox and sealed with polyimide tape. The diffraction patterns were analysed using Fityk (version 0.9.0; Marcin Wojdyr, 2010). The peaks were fitted to a SplitPearson7 function, and the crystallite size was calculated from the full-width half-maximum of the fitted curve, using the Scherrer equation, to the most intense and not overlapped reflections; Cu: 43.5° ($hkl = 111$), ZnO: 47.5° ($hkl = 102$), 57.2° ($hkl = 110$). For the detailed XRD study of the (101) ZnO nanoparticle peak, the diffraction scans were performed using the same diffractometer with a step size of 0.0167° 2θ, scan step time of 120 s and scan range of 32–38° 2θ. The expansion/contraction of the ZnO lattice was determined, using Bragg's equation, from the position of the (101) peak which was determined by Gaussian fit of the diffraction peak. UV-Vis absorption spectra of ZnO nanoparticles were recorded using a PerkinElmer Lambda 950 spectrometer, in transmission mode, from 300–500 nm with a scan speed of 1 nm s^{-1}. Fourier transform infrared (FT-IR) spectra were recorded using a PerkinElmer Spectrum 100 spectrometer fitted with an ATR attachment and each spectrum was collected with 32 scans, at a resolution of 4 cm^{-1}. Thermogravimetric analysis (TGA) was carried out using a Mettler Toledo TGA/DSC 1, under a flow of dry N_2 at 60 mL min^{-1}, from 100–700 °C, at a heating rate of 5 °C min^{-1}.

Bright field (BF) TEM and HAADF-STEM images were acquired with Johnson Matthey's probe corrected ARM200F, at the ePSIC facility (Diamond Light Source), with an acceleration voltage of 200 keV. Measurement conditions were a CL aperture of 30 μm, convergence semiangle of 24.3 mrad, beam current of 12 pA, and scattering angles of 0–10 and 35–110 mrad, for BF and HAADF-STEM respectively.

XPS was performed on a Thermo Scientific Kα^+ X-ray photoelectron spectrometer system operating at 2×10^{-9} mbar base pressure. This system incorporates a monochromated, microfocused Al Kα X-ray source ($h\nu = 1486.6$ eV) and a 180° double focusing hemispherical analyser with a 2D detector. The X-ray source was operated at 6 mA emission current and 12 kV anode bias and a flood gun was used to minimize sample charging. Samples were mounted using conductive carbon tape and transferred to the spectrometer, using a special glovebox module, which ensured that samples were transferred without exposure to air. Data were collected at 20 eV pass energy for core levels and Auger lines. Data were collected over six measurement positions using an X-ray spot size of 400 μm to avoid beam damage affecting the results. Data were then averaged across the different measurement positions. All data were analysed using the Avantage software package.

Synthesis of ZnO@DOPA.[9,40] Dioctylphosphinic acid (200 mg, 0.69 mmol) was added to a Schlenk flask, with a stirrer bar, and the flask was subjected to vacuum for 2 h. Toluene (23 mL) was added to the flask and diethylzinc (425 mg, 3.45 mmol) was added dropwise to the solution. The mixture was stirred overnight under N_2. A 0.4 M solution of HPLC-grade water (123 mg) in acetone (17.2 mL) was added to the reaction mixture dropwise over a period of 8 min. Upon the addition of H_2O in acetone, the mixture went from a colourless solution, *via* a white gel-phase, to a white suspension and the mixture was stirred for 2 h. The white precipitate was isolated by centrifugation (3900 rpm, 20 min), re-dissolved in toluene (3 mL), re-precipitated with acetone (12 mL), and finally washed with acetone only; with centrifugation being applied after each washing-precipitation step. The white precipitate was left to air-dry overnight, yielding ZnO@DOPA as a white powder.

Synthesis of M:ZnO@DOPA (M = Mg, Al, Cu). Dioctylphosphinic acid (200 mg, 0.69 mmol) was added to a Schlenk flask, with a stirrer bar, and the flask was subjected to vacuum for 2 h. Toluene (23 mL) was added to the flask. Diethylzinc (404 mg, 3.27 mmol) was added dropwise to the solution, followed by the addition of the dopant precursor Mg(^{n}Bu)(^{s}Bu), $AlEt_3$ or CuMes (0.172 mmol, amounts of doping reagent added are found in Table S1†). The mixture was stirred overnight under N_2. A 0.4 M solution of HPLC-grade water (123 mg) in acetone (17.2 mL) was added to the reaction mixture dropwise over a period of 8 min. Upon the addition of water in acetone, the mixture went from a colourless solution, *via* a white gel-phase, to a white (or green for Cu-doping) suspension and the mixture was stirred for 2 h. The separation of the precipitate was achieved through centrifugation (3900 rpm, 20 min) and then the precipitate was re-dissolved in toluene (3 mL) and re-precipitated with acetone (12 mL), and finally washed with acetone only. Centrifugation was applied after each washing-precipitation step. The precipitate was left to air-dry overnight, yielding Mg:ZnO@DOPA (0.426 g, 87% based on Zn) and Al:ZnO@DOPA (0.440 g, 89% based on Zn) as white powders and a dark green powder for Cu:ZnO@DOPA (0.438 g, 92% based on Zn).

Synthesis of Cu@DOPA.[64] Mesitylcopper (73.3 mg, 0.40 mmol) and dioctylphosphinic acid (11.7 mg, 0.04 mmol) were dissolved in mesitylene (11 mL) in a 50 mL Young's ampoule and the overall [CuMes] was 0.036 M. The mixture was stirred for 10 min before two freeze–pump–thaw cycles were performed. H_2 gas was charged into the flask whilst the flask was under vacuum and submerged in liquid nitrogen (at room temperature, this loading equates to 2 bar of H_2). The reaction mixture was thawed and warmed to room temperature before being heated to 110 °C for 2.5 h, yielding a deep red solution. The solution was cooled to room temperature and the H_2 gas was removed by 4 cycles of short vacuum/N_2 (care must be taken not to remove solvent during this degassing process). The deep red Cu@DOPA solution was then used in the catalytic hydrogenation of CO_2 to methanol, alongside ZnO@DOPA or M:ZnO@DOPA.

Catalytic CO_2 hydrogenation to methanol. The methanol synthesis from CO_2 experiments were conducted in the same manner as previously described.[40] A 300 mL continuous flow stirred-tank reactor (CSTR, Parr) was used, with stirring speed of 1500 rpm and vertical baffles to ensure homogeneous mixing of the liquid and gas phase. Air-stable ZnO or M : ZnO nanoparticles were added directly to the reactor vessel together with mesitylene (89 mL). The solution was stirred and degassed by a flow of N_2 (600 mL min^{-1}) for 30 min. The air-sensitive Cu@DOPA colloid was introduced into the reactor using a syringe under a flow of N_2, giving a total reactor volume of 100 mL. A Zn : Cu ratio of 1 : 1 (0.4 mmol each) was added in all cases. The reactor was then pressurised to 50 bar using a gas mixture of 96 vol% of $H_2 : CO_2 = 3 : 1$ and 4 vol% Ar (used as internal standard for GC analysis), and heated to 210 °C. The experiments were performed at a flow rate of 150 mL min^{-1} for 20 h. The stability study with Al:ZnO@DOPA was performed at a flow rate of 150 mL min^{-1} for 40 h.

The commercial CuO–ZnO–Al_2O_3 catalyst was obtained from Alfa Aesar (45 776, pellet size 5.4 × 3.6 mm, mass composition CuO, 63.5%; ZnO, 25.1%; Al_2O_3, 10.1%; MgO, 1.3%). It was ground to a fine powder and tested as a reference material. The choice of catalyst loading was dictated by the normalisation considerations, making sure that the total molar concentration of Cu and Zn was the same as in the Cu/ZnO colloids. The catalyst is pre-activated using a diluted H_2 stream (5 vol% H_2/N_2) at 4.5 bar and 240 °C (ramp 2 °C min^{-1}) for 3 h, according to a standard activation protocol for the ternary Cu–ZnO–Al_2O_3 methanol synthesis catalyst in a slurry reactor.[65] The catalytic runs were performed under the conditions stated above.

The reaction products and unreacted material were monitored by an online gas chromatograph (Bruker 450 GC), equipped with a thermal conductivity detector (TCD) and a flame ionisation detector (FID). TCD was used to quantify CO, CO_2 and Ar, whilst FID was used to quantify methanol and other oxygenates or hydrocarbons. The lines from the reactor to the GC were heated to 180 °C to avoid the condensation of any products. All experiments were conducted under differential conditions, with an overall CO_2 conversion <2%, avoiding mass transport limitations (see ESI† for details). Selectivity values are given on a carbon basis, where the only two products were methanol and CO.

Results and discussion

Synthesis and characterisation of M:ZnO@DOPA

Small (2–3 nm) colloidal ZnO nanoparticles (ZnO@DOPA) were previously prepared by the controlled hydrolysis of diethylzinc and sub-stoichiometric amounts (*vs.* $ZnEt_2$) of DOPA–H, in a molar ratio of Zn : DOPA–H = 5 : 1.[9,40] The $[DOPA]^-$ ligand stabilises the nanoparticles and results in high solubility in organic solvents.[9,40,57] Here, this general hydrolysis procedure was applied to doped-ZnO nanoparticles by the reaction of $ZnEt_2$ with the desired dopant organometallic precursors (MR_x) prior to hydrolysis. Three dopants were targeted as they either showed precedent for acting as structural and/or electronic promoters (Mg(II) and Al(III))[28,29,32,66,67] or are required for the highly investigated Cu–ZnO synergy (Cu(I)),[24,28,29,36,37,68–75] which is proposed to be critical in methanol synthesis.

In each case, a pre-hydrolysis mixture was obtained by reacting 0.2 equiv. of DOPA–H with commercially available diethylzinc (0.95 equiv.) and 0.05 equiv. of commercially available (*n*-butyl)(*sec*-butyl)magnesium, triethylaluminium or mesitylcopper (CuMes) in toluene. These precursors were selected not only due to their availability, but also high solubility in organic solvents and rapid reactivity with water to deter phase separation between zinc and dopant. The overall metal : ligand ratio was maintained at 5 : 1 as these conditions yielded particles fully saturated with ligand. Upon reaction with water, the organometallic reagents produce only inert hydrocarbons as byproducts (*i.e.* ethane, butane and/or mesitylene, respectively) which are easily removed from the final product *in vacuo*. The post-hydrolysis mixture, consisting of a colloidal suspension of ZnO nanoparticles, was purified by reducing the solvent volume and *via* centrifugation, yielding Mg:ZnO@DOPA and Al:ZnO@DOPA as white powders and Cu:ZnO@DOPA as a dark green powder.

Analysis of the as-synthesised particles by X-ray diffraction (XRD) showed the formation of small crystalline particles (2–3 nm) with sizing determined *via* peak analysis using the Scherrer equation (Table 1). In each case, only the wurtzite ZnO phase was observed (Fig. 1a–d), suggesting incorporation of any dopants into the crystalline structure rather than co-crystallisation of other phases. High-angle angular dark-field scanning tunnelling electron microscopy (HAADF-STEM) images (Fig. 1e–g) revealed spherical nanoparticles with narrow size distributions (2.6–2.8 nm, Fig. S1†) and no obvious amorphous phases were observed by electron microscopy.

Incorporation of the second metal was assessed further, by considering changes to the lattice parameters, evidenced in the strongest (101) reflection (Table 1, Fig. S2†). A significant contraction was observed in Al:ZnO@DOPA, indicative of successful substitution of tetrahedral Zn(II) sites ($r_{ion}[Zn(II)] = 0.74$ Å) with Al(III) ($r_{ion}[Al(III)] = 0.53$ Å).[76,77] No clear lattice changes were observed for Mg:ZnO@DOPA and Cu:ZnO@DOPA due to the similar ionic radii of the metals ($r_{ion}[Mg(II)] = 0.71$ Å and $r_{ion}[Cu(I)] = 0.74$ Å) and the peak breadth resulting from the small particle sizes.[14,78]

Bulk compositional analysis by ICP-OES confirmed and quantified the presence of the dopants. For Al:ZnO@DOPA and Cu:ZnO@DOPA, the heteroatom concentration of 5 mol% is in line with starting reagent stoichiometry, but the value for Mg:ZnO@DOPA is slightly lower than expected (Table 2). The solid-state[27] Al-MAS-NMR spectrum of Al:ZnO@DOPA (Fig. S3†) confirms the replacement of tetrahedral Zn(II) with Al(III), indicated by the sharp signal at δ 55 ppm which corresponds to tetrahedral Al(III) environments. In addition, pentahedral (δ_{Al}:

Table 1 Table showing the sizes and (101) peak information for ZnO@DOPA and M:ZnO@DOPA

	Size (nm)		(101) reflection[c]		
M : ZnO samples	XRD[a]	TEM[b]	2θ°	d Å^{-1}	Δd Å^{-1}
ZnO@DOPA	2.3	2.8 ± 0.02 (0.6)	34.62	2.59	—
Mg:ZnO@DOPA	2.0	2.7 ± 0.04 (0.5)	34.31	2.61	+0.02
Al:ZnO@DOPA	2.3	2.7 ± 0.06 (0.9)	35.75	2.51	−0.08
Cu:ZnO@DOPA	2.2	2.6 ± 0.03 (0.4)	34.82	2.58	−0.01

[a] Average particle size determined by application of the Scherrer equation to XRD (102) and (110) reflections (Fig. 1a–d). [b] Average particle size ± standard error (standard deviation) determined by size analysis of TEM images (Fig. 1e–f). The standard error of the mean is defined as standard deviation/(no. of measurements). [c] The positions of (101) peaks were determined using Gaussian fits to the XRD reflection in the range of 30–35° 2θ (Fig. S2).

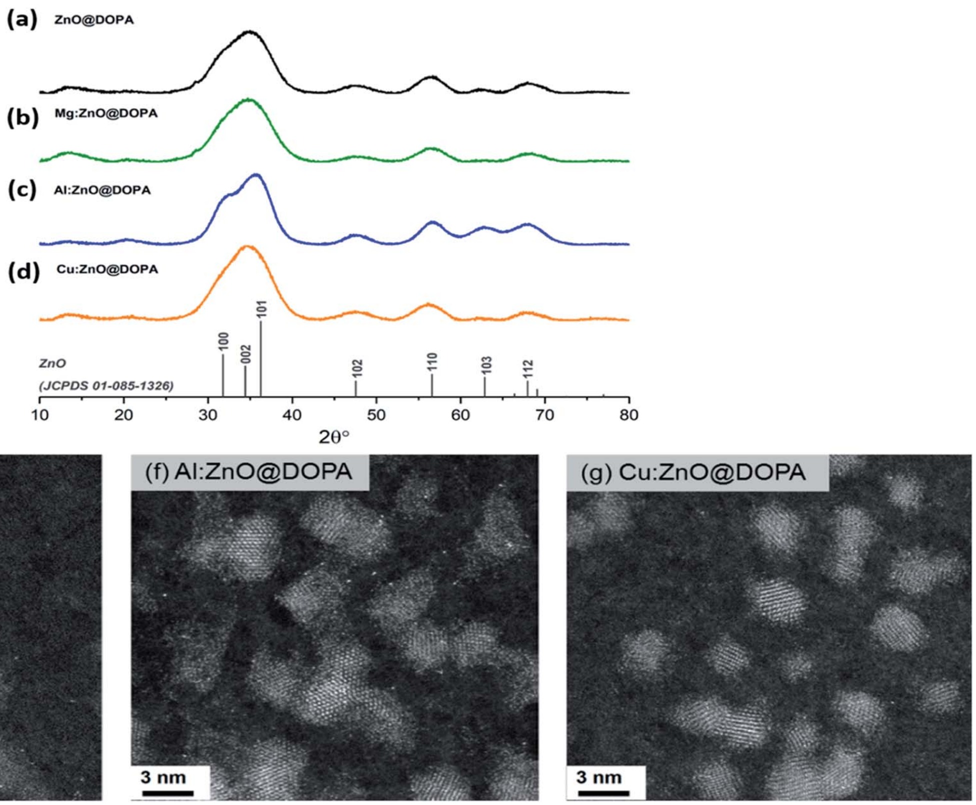

Fig. 1 Powder XRD patterns and HAADF-STEM images of (a) ZnO@DOPA, (b) & (e) Mg:ZnO@DOPA, (c) & (f) Al:ZnO@DOPA and (d) & (g) Cu:ZnO@DOPA. Patterns are indexed against ZnO as grey vertical bars (JCPDS 01-085-1326). All scale bars in the STEM images are 3 nm.

Table 2 Table showing the dopant quantities, obtained by ICP-OES and XPS, and optical band-gaps of ZnO@DOPA, Mg:ZnO@DOPA, Al:ZnO@DOPA and Cu:ZnO@DOPA, obtained from Tauc plots (Fig. S4)

	Dopant quantity (rel. at%)		Optical band-gap (eV)
M:ZnO@DOPA	ICP-OES	XPS	UV-Vis[c]
ZnO@DOPA	—	—	3.71
Mg:ZnO@DOPA	3.77 ± 0.05	4.5[a]	3.84
Al:ZnO@DOPA	4.96 ± 0.07	5.0[b]	3.65
Cu:ZnO@DOPA	5.05 ± 0.07	3.3[a]	3.67

[a] Derived from comparison of the peak area from peak fit analysis of Zn $2p_{3/2}$ with Cu $2p_{3/2}$ and Mg 1s (Fig. 2). Error of ±0.5%. [b] Derived from comparison of the peak area from peak fit analysis of Zn 3s with Al 2p (Fig. 2). Error of ±0.5%. [c] Error of ±0.04 eV, derived from uncertainty of linear fits (coefficient of determination, $R^2 > 0.99$) (Fig. S4).[28]

47 ppm) and octahedral (δ_{Al}: −17 and 16 ppm) Al environments are also present and are tentatively assigned as surface sites.[28,66,67]

The chemical environments and oxidation states for all samples were analysed using XPS (Fig. 2). All samples show a binding energy (BE) for Zn $2p_{3/2}$ at 1021.7 eV, however from the Zn core level alone, it is not possible to determine its oxidation state, as the BEs of Zn metal and ZnO are identical.[79] However, the Zn $L_3M_{4,5}M_{4,5}$ Auger lines clearly show the typical structure of ZnO, with two features at 987.9 eV and 991.1 eV kinetic energy (KE). The P 2p and C 1s lines show BEs expected for the DOPA ligand. The O 1s core level has two contributions, one from ZnO at 530.4 eV and one at 531.5 eV from DOPA.[80] The Mg 1s and Al 2p core level appear at BEs typical for Mg(II) and Al(III), 1304.2 eV and 73.9 eV, respectively. The Cu $2p_{3/2}$ core level is at a BE of 932.3 eV, which can either stem from Cu(0) or Cu(I).[81] Usually, the Cu LMM Auger lines can be used to distinguish between these two oxidation states, but in these samples, the lines overlap with the much stronger Zn LMM lines, preventing further analysis. The core level also exhibits a small shoulder towards higher BE, at 933.7 eV, indicating a small amount of Cu(II). From peak fit analysis of the Zn $2p_{3/2}$ and the metal core levels, relative atomic ratios were determined (Table 2). Comparing the dopant quantities obtained by XPS and ICP-OES highlights the likely surface speciation of Mg, compared to Al which appears to be distributed throughout the particles.

The optical band-gaps were determined *via* Tauc plots from the on-set absorption in solid-state UV-Vis spectra (Table 2, Fig. S4†). The Al-doped sample showed a smaller band-gap than ZnO, presumably due to the introduction of Al(III) additional donor levels.[11,82–84] In contrast, Mg(II) doping widens the band-gap, as observed by others.[14,28,78,85–87] A small decrease in the band-gap of Cu:ZnO@DOPA (3.67 eV) suggests partial incorporation of Cu(I)/Cu(II) into the lattice, where the dopant provides additional shallow acceptor levels,[88,89] as a larger decrease would be expected for 5% doping.[90] It is possible that

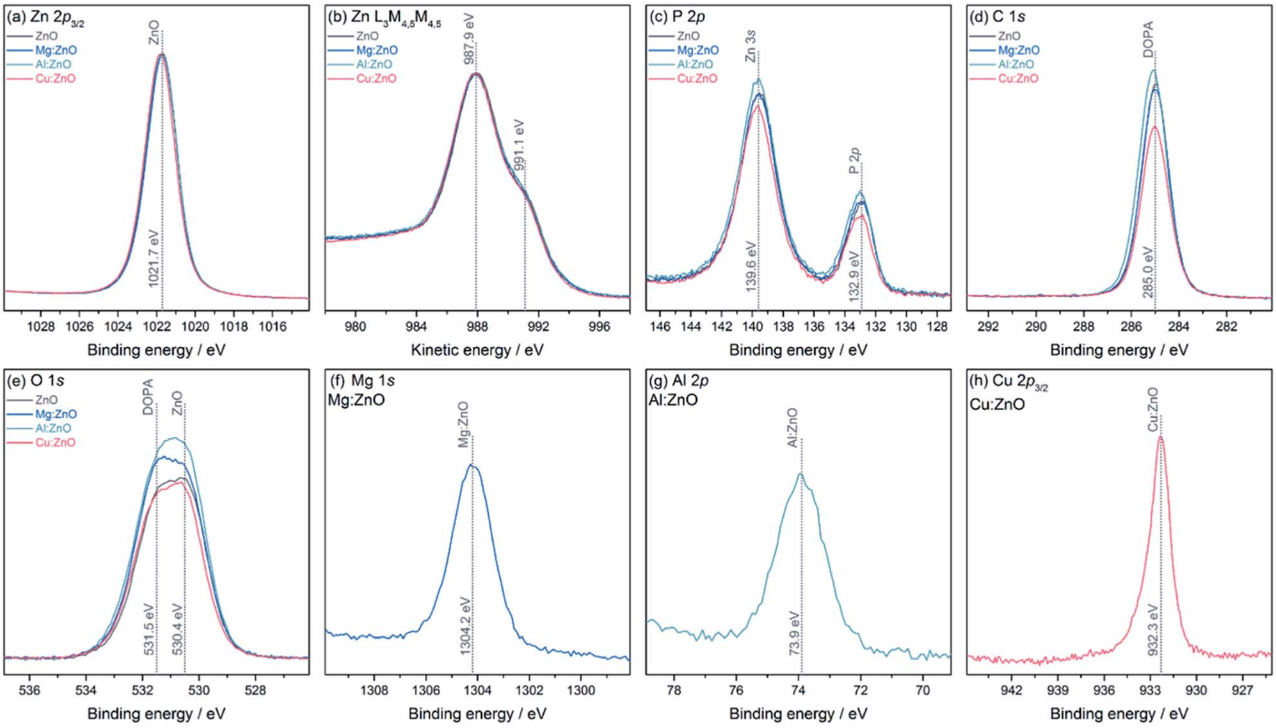

Fig. 2 XPS core levels and Auger spectra for ZnO@DOPA and M:ZnO@DOPA samples, including (a) Zn $2p_{3/2}$, (b) Zn $L_3M_{4,5}M_{4,5}$ (c) P 2p/Zn 3s, (d) C 1s, (e) O 1s, and (f) Mg 1s of Mg:ZnO@DOPA, (g) Al 2p of Al:ZnO@DOPA, and (h) Cu $2p_{3/2}$ of Cu:ZnO@DOPA.

some of the CuMes is also reduced to Cu(0), rather than doping the ZnO. It was previously reported that CuMes reacts with diethylzinc to produce Cu(0) nanoparticles.[41] In this work, however, there was no direct evidence for such small Cu(0) nanoparticles by TEM or XRD.

Analysis of all the new nanoparticles by TGA showed a mass loss of 25–30% between 150–500 °C for all M:ZnO@DOPA, assigned to the thermal decomposition of the $[DOPA]^-$ ligand (Table S2, Fig. S5†). Along with elemental analysis (Table S2†), ratios close to M:ZnO : $[DOPA]^-$ = 6 : 1 were found for M:ZnO@DOPA. The ratio differs slightly to the starting reagent stoichiometry and it is proposed that low quantities of soluble molecular clusters *e.g.* $[Zn_4O(DOPA)_6]$, are removed during nanoparticle purification and account for the lower ligand loading.[57]

From IR spectroscopy (Fig. S6†), the presence of C–H stretches (2800–3000 cm^{-1}), along with phosphinate, PO_2^-, stretches (~1047 cm^{-1}, asymm; ~1126 cm^{-1}, symm) associated with the ligand were detected. The separation of 79–81 cm^{-1} between the asymmetric and symmetric phosphinate stretches indicates κ^2-ligand coordination (see Fig. S6† inset). The presence of O–H stretches centred at 3380 cm^{-1}, is indicative of hydroxyl and water coordinated to the nanoparticle surface. Overall, all characterisation data strongly suggest the successful incorporation of Mg(II) and Al(III) into the lattice of ZnO nanoparticles, whilst Cu(I) appears to have been partially incorporated.

Catalytic CO_2 hydrogenation to methanol

The M:ZnO@DOPA nanoparticles were combined with colloidal Cu@DOPA nanoparticles and tested as catalysts for the hydrogenation of CO_2 to methanol (Fig. 3), under differential conditions (CO_2 conversion <2%). A short residence time allowed accurate calculation of reaction rates, avoiding complications due to competing side reactions such as the rWGS reaction. Cu@DOPA nanoparticles were synthesised by the hydrogenation of CuMes in the presence of DOPA–H and detailed characterisation data are consistent with previous reports (Cu : DOPA–H = 10 : 1).[64,91] For each catalytic experiment, the colloidal catalysts (0.4 mmol Cu and 0.4 mmol M:Zn@DOPA) were introduced into the continuous flow stirred tank reactor with mesitylene as solvent (total of 100 mL), under a dynamic flow of nitrogen. Mesitylene was selected on the basis of its non-coordinating nature and high boiling point (165 °C),

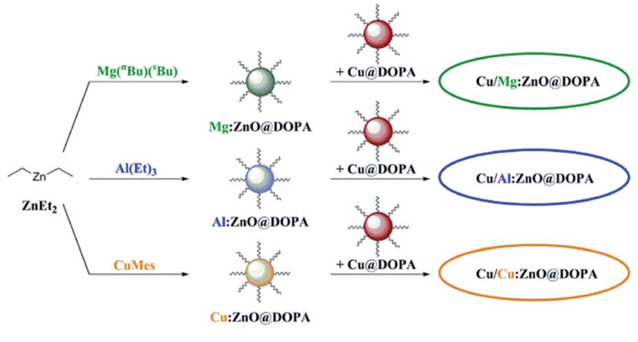

Fig. 3 Overview of M:ZnO@DOPA syntheses and the subsequent combination with Cu@DOPA for the formation of colloidal Cu/ZnO nanocatalysts in hydrogenation of CO_2 to methanol.

while being sufficiently volatile to allow for its complete removal under vacuum for analysis of spent catalysts. The reactor was pressurised to 50 bar with a gas feed of a $CO_2 : H_2$ mixture (molar ratio of 1 : 3), at 210 °C, following previous protocols.[39,70] Established colloidal Cu/ZnO@DOPA and the commercial heterogeneous catalyst Cu–ZnO–Al_2O_3 were also tested as benchmarks for this study. The activation of heterogeneous Cu–ZnO–Al_2O_3 was conducted following a standard procedure.[65]

All catalysts reached peak methanol production rate after 3–4 h time-on-stream and remained stable for over 15 h (Fig. S7 and S8†). High methanol selectivity was observed in all cases and CO was the only by-product (from the rWGS reaction). Both doped and undoped colloidal catalysts displayed higher activities than the commercial heterogeneous catalyst (Fig. 4). Mg-doping was somewhat detrimental to activity in comparison with undoped ZnO@DOPA; Cu/Mg:ZnO@DOPA displays 30–40% lower activity than the other three colloidal catalysts. Cu/Al:ZnO@DOPA showed a small but noticeable improvement when compared to Cu/ZnO@DOPA (+10%), but no clear difference was observed for the Cu-doped sample.

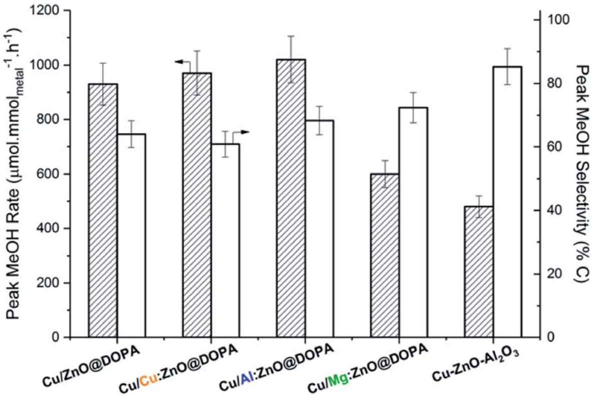

Fig. 4 Peak methanol rates and selectivity for the colloidal Cu/ZnO@DOPA, Cu/M:ZnO@DOPA catalysts and reference catalyst Cu–ZnO–Al_2O_3 in the hydrogenation of CO_2 to methanol. Reaction conditions: 210 °C, 50 bar, $CO_2 : H2 = 1 : 3$, 150 mL min^{-1}.

All post-catalysis colloids were characterised using air-sensitive techniques to prevent the oxidation of Cu(0). By XRD, all samples displayed typical diffraction peaks attributed to crystalline ZnO and metallic Cu(0), with no additional crystalline phases observed (Fig. S9–S11†). Some ripening of the original M:ZnO@DOPA and Cu(0) nanoparticles was indicated by XRD and TEM (Table 3).

The difference in activity between the highest (Al-doped) and lowest (Mg-doped) samples is tentatively attributed to the quantity of Cu/ZnO interfaces. These interfaces, formed under the reductive catalytic conditions, are commonly suggested to be the active site for methanol synthesis. They can be identified using electron microscopy, through analysis of the degree of contact between different identifiable crystalline phases.[36,37,46,68,69] To this end, the nanoscale structures of post-catalysis samples of Cu/Mg:ZnO@DOPA and Cu/Al:ZnO@DOPA were investigated using BF-TEM, and were found to differ significantly.

Cu/Al:ZnO@DOPA showed contact between Cu and Al:ZnO nanoparticles (Fig. 5a & S13†). The nanocrystalline particles were additionally surrounded by an amorphous network that is rich in Al(III) (identified by EDX) and likely to be alumina as suggested by the emergence of a second, higher BE species (76.8 eV) in the Al 2p core line by XPS (Fig. S12 & S13†). The formation of surface alumina under reducing conditions has also been found in the heterogeneous Cu–ZnO–Al_2O_3 catalyst. In this case it appears the Al(III) that remains within the lattice acts as an electronic promoter, while the *in situ* formed alumina matrix acts as a structural promoter.[28,29,67] It is proposed that Al-doping of ZnO increases the density of donor states (n-type) and contributes to the formation of oxygen vacancies which accelerates migration of Zn onto Cu(0) and hence increases the formation of Cu/ZnO interfaces.[71–73]

More isolated nanoparticles and fewer Cu/ZnO interfaces were observed for Cu/Mg:ZnO@DOPA (Fig. 5b & S14†). Additionally, the Mg-rich surface of Mg:ZnO@DOPA (as suggested by XPS) might hinder ZnO and Cu(0) interface formation. EDX of the post-catalysis sample shows that some Mg is distributed in between Cu(0) and ZnO nanoparticles (Fig. S14†). It appears Mg(II) is detrimental to activity as both a structural and electronic dopant.

Table 3 Cu(0) and ZnO nanoparticles size data from XRD and TEM for pre-catalysis and post-catalysis colloids (20 h time-on-stream, unless otherwise specified)

	ZnO (nm)				Cu[f] (nm)	
	Pre-catalysis		Post-catalysis		Post-catalysis	
Catalyst	XRD[a]	TEM[b]	XRD[a]	TEM[b]	XRD[a]	TEM[b]
Cu/ZnO@DOPA[c]	2.3	2.8 ± 0.02 (0.6)	3.2	4.9 ± 0.1 (1.1)	6.4	7.2 ± 0.2 (1.9)
Cu/Mg:ZnO@DOPA	2.0	2.7 ± 0.04 (0.5)	2.3	3.5 ± 0.04 (0.4)	4.4	4.3 ± 0.06 (0.6)
Cu/Al:ZnO@DOPA[d]	2.3	2.7 ± 0.06 (0.9)	3.6 (3.1)[e]	4.5 ± 0.07 (1.3)	3.0 (2.4)[e]	4.6 ± 0.02 (1.1)
Cu/Cu:ZnO@DOPA	2.2	2.6 ± 0.03 (0.4)	3.3	—	2.0	—

[a] Average particle size determined by application of the Scherrer equation to XRD (102) and (110) reflections (Fig. 1a–d and S9–S11). [b] Average particle size ± standard error (standard deviation) determined by size analysis of TEM images (Fig. 1e–f and S14, S15). The standard error of the mean is defined as standard deviation/(no. of measurements). [c] The sizing measurement is taken from previously published system.[40] [d] Measurement taken from 40 h time-on-stream study. [e] Crystallite size of catalyst after 20 h time-on-stream. [f] For pre-catalysis Cu@DOPA, sizes of ~2 nm were reported using TEM.[64]

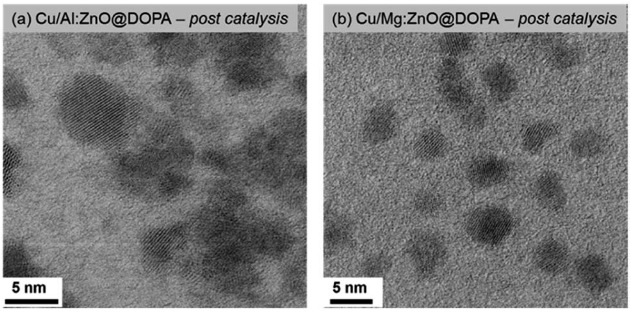

Fig. 5 BF-TEM images of the post-catalysis sample of (a) Cu/Al:ZnO@DOPA and (b) Cu/Mg:ZnO@DOPA.

This is in line with a previous study of Mg(II) doping into the heterogeneous Cu–ZnO–Al_2O_3 methanol catalysts from syn-gas (230 °C, 30 bar, CO : CO_2 : H_2: inert gas = 6 : 8 : 59 : 27).[28]

Stability of the colloidal catalyst

During the 20 h time-on-stream (210 °C, 50 bar, mesitylene), the colloidal catalysts all displayed good short-term stability. In contrast, the commercial heterogeneous catalyst Cu–ZnO–Al_2O_3 was significantly deactivated, by ~15%, over this period. This reduction in activity may be attributed to sintering and agglomeration of Cu(0) under the operating conditions.[92,93] In this sense, CO_2/H_2 is a considerably more demanding feed-gas than syn-gas. In order to explore colloidal catalyst stability over a longer period, the Cu/Al:ZnO@DOPA sample was tested against the heterogeneous catalyst over 40 h (210 °C, 50 bar, 150 mL min^{-1}). Only a small reduction in activity was observed for Cu/Al:ZnO@DOPA (~7%), whereas the Cu–ZnO–Al_2O_3 catalyst experienced ~30% deactivation (Fig. 6 & S15†). With both catalysts, methanol selectivity remained high throughout (Fig. S16†). The better stability of the colloidal catalyst is tentatively attributed to the high particle stability, as post catalysis analysis revealed that agglomeration was significantly prevented. Specifically, the Cu(0) nanoparticles sizes only increase from 2.4 to 3.0 nm and the ZnO from 3.1 to 3.6 nm (Table 3 & Fig. S10†). Whilst the solvated, phosphinate ligand stabilised particles ripen more slowly than the heterogeneous catalyst, the presence of the alumina network may help to decrease the sintering further through structural promotion. CO_2 conversion could likely be increased with longer residence times (lower supplied gas space velocities), but at the expense of rate and methanol selectivity.[38,43] A detailed process study would be needed to optimise any one specific catalyst.

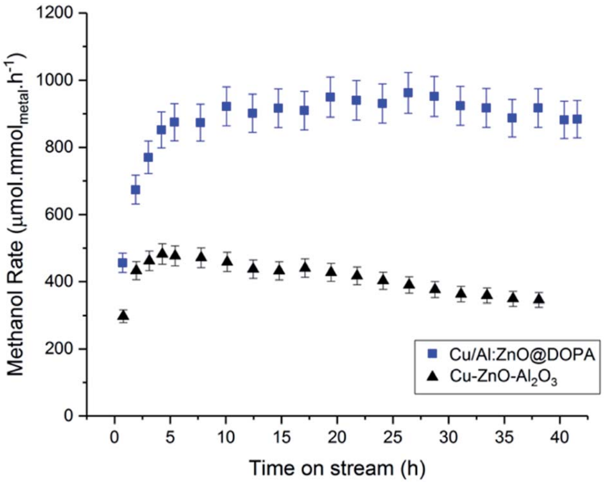

Fig. 6 Methanol rates of Cu/Al:ZnO@DOPA and commercial heterogeneous Cu–ZnO–Al_2O_3, over 40 h time-on-stream.

Conclusions

Doped-ZnO nanoparticles (2–3 nm), with ~5 mol% dopant (Mg(II), Al(III) and Cu(I)), and phosphinate capping ligands, were synthesised by the room temperature hydrolysis of a mixture of organometallic reagents. The particle analysis suggests the localisation of Mg(II) on the surface of the ZnO nanoparticles, whilst Al(III) is distributed throughout the structure. For Cu-doped ZnO, incomplete incorporation of Cu(I) is suggested by the optical band-gap and XPS, probably due to partial Cu(0) formation. UV-Vis spectroscopy showed a smaller band-gap for Al-doping but a larger band-gap for Mg-doped particles compared to ZnO alone.

The doped ZnO nanoparticles were combined with Cu(0) nanoparticles (<2 nm), capped by phosphinate, to form a series of active colloidal nanocatalysts for the hydrogenation of CO_2 to methanol in the liquid phase (210 °C, 50 bar, H_2 : CO_2 molar ratio of 3 : 1, 150 mL min^{-1}). All catalysts showed methanol production rates higher than a benchmark heterogeneous catalyst Cu–ZnO–Al_2O_3, although the Mg-doped catalyst showed ~40% lower activity than the other colloidal catalysts. It is proposed that the Mg rich surface layer prevents formation of catalytically important Cu/ZnO interfaces. In contrast, Al-doping improved activity compared to ZnO nanoparticles. An amorphous surface alumina network is indicated in these post-catalysis samples and may hinder nanoparticle ripening and improve catalyst stability over a 40 h time-on-stream.

The organometallic synthesis of doped colloidal ZnO nanoparticles is a useful means to tune properties and appears to be somewhat generalizable. Future studies should target mixed metal oxides and dopant levels. In particular, transition metal and Group 13 n-type ZnO dopants should be explored, as these materials show promising performances in syn-gas liquid phase methanol synthesis.[26]

Conflicts of interest

There are no conflicts to declare.

Acknowledgements

The Engineering and Physical Sciences Research Council are acknowledged for research funding (EP/H046380/1, EP/K035274/1; DTA studentships to AL). AR acknowledges the support from Imperial College London for her Imperial College Research Fellowship and from the Analytical Chemistry Trust Fund for her CAMS-UK Fellowship. Johnson Matthey PLC is acknowledged for using their aberration corrected JEOL 200F microscope located within the ePSIC facility (Diamond Light Source).

Notes and references

1 R. Buonsanti and D. J. Milliron, *Chem. Mater.*, 2013, **25**, 1305–1317.
2 D. Mocatta, G. Cohen, J. Schattner, O. Millo, E. Rabani and U. Banin, *Science*, 2011, **332**, 77–81.
3 Ü. Özgür, Y. I. Alivov, C. Liu, A. Teke, M. A. Reshchikov, S. Doğan, V. Avrutin, S.-J. Cho and H. Morkoç, *J. Appl. Phys.*, 2005, **98**, 041301.
4 J. A. Garden and S. D. Pike, *Dalton Trans.*, 2018, **47**, 3638–3662.
5 A. M. Schimpf, C. E. Gunthardt, J. D. Rinehart, J. M. Mayer and D. R. Gamelin, *J. Am. Chem. Soc.*, 2013, **135**, 16569–16577.
6 C. N. Valdez, M. Braten, A. Soria, D. R. Gamelin and J. M. Mayer, *J. Am. Chem. Soc.*, 2013, **135**, 8492–8495.
7 J. N. Schrauben, R. Hayoun, C. N. Valdez, M. Braten, L. Fridley and J. M. Mayer, *Science*, 2012, **336**, 1298–1301.
8 A. García-Trenco, E. R. White, M. S. P. Shaffer and C. K. Williams, *Catal. Sci. Technol.*, 2016, **6**, 4389–4397.
9 N. J. Brown, J. Weiner, K. Hellgardt, M. S. P. Shaffer and C. K. Williams, *Chem. Commun.*, 2013, **49**, 11074–11076.
10 S. Sharma, S. S. Pande and P. Swaminathan, *RSC Adv.*, 2017, **7**, 39411–39419.
11 R. Buonsanti, A. Llordes, S. Aloni, B. A. Helms and D. J. Milliron, *Nano Lett.*, 2011, **11**, 4706–4710.
12 Z. Sun, J. He, A. Kumbhar and J. Fang, *Langmuir*, 2010, **26**, 4246–4250.
13 S. T. Ochsenbein and D. R. Gamelin, *Nat. Nanotechnol.*, 2011, **6**, 112–115.
14 A. W. Cohn, K. R. Kittilstved and D. R. Gamelin, *J. Am. Chem. Soc.*, 2012, **134**, 7937–7943.
15 S. Polarz, A. Orlov, A. Hoffmann, M. R. Wagner, C. Rauch, R. Kirste, W. Gehlhoff, Y. Aksu, M. Driess, M. W. E. van den Berg and M. Lehmann, *Chem. Mater.*, 2009, **21**, 3889–3897.
16 Y. Kanai, *Jpn. J. Appl. Phys.*, 1991, **30**, 703–707.
17 C. Rauch, W. Gehlhoff, M. R. Wagner, E. Malguth, G. Callsen, R. Kirste, B. Salameh, A. Hoffmann, S. Polarz, Y. Aksu and M. Driess, *J. Appl. Phys.*, 2010, **107**, 024311.
18 S. B. Zhang, S.-H. Wei and A. Zunger, *Phys. Rev. B: Condens. Matter Mater. Phys.*, 2001, **63**, 1–7.
19 K. Mohanta, S. K. Batabyal and A. J. Pal, *Chem. Mater.*, 2007, **19**, 3662–3666.
20 R. Frisenda, A. J. Molina-Mendoza, T. Mueller, A. Castellanos-Gomez and H. van der Zant, *Chem. Soc. Rev.*, 2018, **47**, 3339–3358.
21 C. Baltes, S. Vukojević and F. Schüth, *J. Catal.*, 2008, **258**, 334–344.
22 A. Galadima and O. Muraza, *J. Nat. Gas Sci. Eng.*, 2015, **25**, 303–316.
23 L. C. Grabow and M. Mavrikakis, *ACS Catal.*, 2011, **1**, 365–384.
24 S. Natesakhawat, J. W. Lekse, J. P. Baltrus, P. R. Ohodnicki Jr, B. H. Howard, X. Deng and C. Matranga, *ACS Catal.*, 2012, **2**, 1667–1676.
25 M. Saito and K. Murata, *Catal. Surv. Asia*, 2004, **8**, 285–294.
26 W. Wang, S. Wang, X. Ma and J. Gong, *Chem. Soc. Rev.*, 2011, **40**, 3703–3727.
27 H. Y. Chen, J. Lin, K. L. Tan and J. Li, *Appl. Surf. Sci.*, 1998, **126**, 323–331.
28 J. Schumann, M. Eichelbaum, T. Lunkenbein, N. Thomas, M. C. Á. Galván, R. Schlögl and M. Behrens, *ACS Catal.*, 2015, **5**, 3260–3270.
29 M. Behrens, S. Zander, P. Kurr, N. Jacobsen, J. Senker, G. Koch, T. Ressler, R. W. Fischer and R. Schlögl, *J. Am. Chem. Soc.*, 2013, **135**, 6061–6068.
30 G. A. Vedage, P. B. Himelfarb, G. W. Simmons and K. Klier, in *Solid State Chemistry in Catalysis*, American Chemical Society, 1985, ch. 18, vol. 279, pp. 295–312.
31 C. Li, X. Yuan and K. Fujimoto, *Appl. Catal., A*, 2014, **469**, 306–311.
32 J. G. Nunan, P. B. Himelfarb, R. G. Herman, K. Klier, C. E. Bogdan and G. W. Simmons, *Inorg. Chem.*, 1989, **28**, 3868–3874.
33 M. M.-J. Li, Z. Zeng, F. Liao, X. Hong and S. C. E. Tsang, *J. Catal.*, 2016, **343**, 157–167.
34 P. L. Hansen, J. B. Wagner, S. Helveg, J. R. Rostrup-Nielsen, B. S. Clausen and H. Topsøe, *Science*, 2002, **295**, 2053–2055.
35 M. B. Fichtl, J. Schumann, I. Kasatkin, N. Jacobsen, M. Behrens, R. Schlögl, M. Muhler and O. Hinrichsen, *Angew. Chem., Int. Ed.*, 2014, **53**, 7043–7047.
36 M. Behrens, F. Studt, I. Kasatkin, S. Kühl, M. Hävecker, F. Abild-Pedersen, S. Zander, F. Girgsdies, P. Kurr, B.-L. Kniep, M. Tovar, R. W. Fischer, J. K. Nørskov and R. Schlögl, *Science*, 2012, **336**, 893–897.
37 J. C. Frost, *Nature*, 1988, **334**, 577–580.
38 M. Sahibzada, I. S. Metcalfe and D. Chadwick, *J. Catal.*, 1998, **174**, 111–118.
39 S. Lee and A. Sardesai, *Top. Catal.*, 2005, **32**, 197–207.
40 S. D. Pike, A. García-Trenco, E. R. White, A. H. M. Leung, J. Weiner, M. S. P. Shaffer and C. K. Williams, *Catal. Sci. Technol.*, 2017, **7**, 3842–3850.
41 N. J. Brown, A. García-Trenco, J. Weiner, E. R. White, M. Allinson, Y. Chen, P. P. Wells, E. K. Gibson, K. Hellgardt, M. S. P. Shaffer and C. K. Williams, *ACS Catal.*, 2015, **5**, 2895–2902.
42 A. García-Trenco, E. R. White, A. Regoutz, D. J. Payne, M. S. P. Shaffer and C. K. Williams, *ACS Catal.*, 2017, **7**, 1186–1196.
43 A. García-Trenco, A. Regoutz, E. R. White, D. J. Payne, M. S. P. Shaffer and C. K. Williams, *Appl. Catal., B*, 2018, **220**, 9–18.
44 M. K. Schröter, L. Khodeir, M. W. E. van den Berg, T. Hikov, M. Cokoja, S. Miao, W. Grünert, M. Muhler and R. A. Fischer, *Chem. Commun.*, 2006, 2498–2500.
45 S. Schimpf, A. Rittermeier, X. Zhang, Z.-A. Li, M. Spasova, M. W. E. van den Berg, M. Farle, Y. Wang, R. A. Fischer and M. Muhler, *ChemCatChem*, 2010, **2**, 214–222.

46 M. A. Sliem, S. Turner, D. Heeskens, S. B. Kalidindi, G. V. Tendeloo, M. Muhler and R. A. Fischer, *Phys. Chem. Chem. Phys.*, 2012, **14**, 8170–8178.

47 C. Kiener, M. Kurtz, H. Wilmer, C. Hoffmann, H.-W. Schmidt, J.-D. Grunwaldt, M. Muhler and F. Schüth, *J. Catal.*, 2003, **216**, 110–119.

48 M. Monge, M. L. Kahn, A. Maisonnat and B. Chaudret, *Angew. Chem., Int. Ed.*, 2003, **42**, 5321–5324.

49 D. Prochowicz, K. Sokołowski and J. Lewiński, *Coord. Chem. Rev.*, 2014, **270–271**, 112–126.

50 K. L. Orchard, M. S. P. Shaffer and C. K. Williams, *Chem. Mater.*, 2012, **24**, 2443–2448.

51 D. Lee, M. Wolska-Pietkiewicz, S. Badoni, A. Grala, J. Lewiński and G. De Paëpe, *Angew. Chem., Int. Ed.*, 2019, **131**, 17323–17328.

52 J. Paczesny, M. Wolska-Pietkiewicz, I. Binkiewicz, M. Wadowska, Z. Wróbel, K. Matuła, W. Nogala, J. Lewiński and R. Hołyst, *ACS Appl. Mater. Interfaces*, 2016, **8**, 13532–13541.

53 J. Paczesny, M. Wolska-Pietkiewicz, I. Binkiewicz, Z. Wróbel, M. Wadowska, K. Matuła, I. Dzięcielewski, D. Pociecha, J. Smalc-Koziorowska, J. Lewiński and R. Hołyst, *Chem.–Eur. J.*, 2015, **21**, 16941–16947.

54 M. Wolska-Pietkiewicz, A. Grala, I. Justyniak, D. Hryciuk, M. Jędrzejewska, J. Grzonka, K. J. Kurzydłowski and J. Lewiński, *Chem.–Eur. J.*, 2017, **23**, 11856–11865.

55 M. Wolska-Pietkiewicz, K. Tokarska, A. Grala, A. Wojewódzka, E. Chwojnowska, J. Grzonka, P. J. Cywiński, K. Kruczała, Z. Sojka, M. Chudy and J. Lewiński, *Chem.–Eur. J.*, 2018, **24**, 4033–4042.

56 M. L. Kahn, M. Monge, V. Collière, F. Senocq, A. Maisonnat and B. Chaudret, *Adv. Funct. Mater.*, 2005, **15**, 458–468.

57 S. D. Pike, E. R. White, M. S. P. Shaffer and C. K. Williams, *Nat. Commun.*, 2016, **7**, 1–11.

58 T. Chen and V. O. Rodionov, *ACS Catal.*, 2016, **6**, 4025–4033.

59 D. L. Hou, X. J. Ye, H. J. Meng, H. J. Zhou, X. L. Li, C. M. Zhen and G. D. Tang, *Appl. Phys. Lett.*, 2007, **90**, 142502.

60 Y. Kanai, *Jpn. J. Appl. Phys.*, 1991, **30**, 2021–2022.

61 C. H. Park, S. B. Zhang and S.-H. Wei, *Phys. Rev. B: Condens. Matter Mater. Phys.*, 2002, **66**, 073202.

62 A. Glaria, M. L. Kahn, T. Cardinal, F. Senocq, V. Jubera and B. Chaudret, *New J. Chem.*, 2007, **32**, 662–669.

63 S. K. Sehmi, S. Noimark, S. D. Pike, J. C. Bear, W. J. Peveler, C. K. Williams, M. S. P. Shaffer, E. Allan, I. P. Parkin and A. J. MacRobert, *ACS Omega*, 2016, **1**, 334–343.

64 S. D. Pike, E. R. White, A. Regoutz, N. Sammy, D. J. Payne, C. K. Williams and M. S. P. Shaffer, *ACS Nano*, 2017, **11**, 2714–2723.

65 A. Sawant, M. K. Ko, V. Parameswaran, S. Lee and C. J. Kulik, *Fuel Sci. Technol. Int.*, 1987, **5**, 77–88.

66 S. Miao, R. N. d'Alnoncourt, T. Reinecke, I. Kasatkin, M. Behrens, R. Schlögl and M. Muhler, *Eur. J. Inorg. Chem.*, 2009, 910–921.

67 M. Behrens, G. Lolli, M. Muratova, I. Kasatkin, M. Hävecker, R. N. d'Alnoncourt, O. Storcheva, K. Köhler, M. Muhler and R. Schlögl, *Phys. Chem. Chem. Phys.*, 2013, **15**, 1374–1381.

68 F. Liao, Y. Huang, J. Ge, W. Zheng, K. Tedsree, P. Collier, X. Hong and S. C. E. Tsang, *Angew. Chem., Int. Ed.*, 2011, **50**, 2162–2165.

69 F. Liao, Z. Zeng, C. Eley, Q. Lu, X. Hong and S. C. E. Tsang, *Angew. Chem., Int. Ed.*, 2012, **51**, 5832–5836.

70 X.-M. Liu, G. Q. Lu, Z.-F. Yan and J. Beltramini, *Ind. Eng. Chem. Res.*, 2003, **42**, 6518–6530.

71 A. le Valant, C. Comminges, C. Tisseraud, C. Canaff, L. Pinard and Y. Pouilloux, *J. Catal.*, 2015, **2015**, 41–49.

72 C. Tisseraud, C. Comminges, T. Belin, H. Ahouari, A. Soualah, Y. Pouilloux and A. le Valant, *J. Catal.*, 2015, **330**, 533–544.

73 C. Tisseraud, C. Comminges, S. Pronier, Y. Pouilloux and A. le Valant, *J. Catal.*, 2016, **343**, 106–114.

74 Y. Choi, K. Futagami, T. Fujitani and J. Nakamura, *Appl. Catal., A*, 2001, **208**, 163–167.

75 J. Nakamura, Y. Choi and T. Fujitani, *Top. Catal.*, 2003, **22**, 277–285.

76 R. D. Shannon, *Acta Crystallogr., Sect. A: Cryst. Phys., Acta Crystallogr., Sect. A: Cryst. Phys., Diffr., Theor. Gen. Crystallogr.*, 1976, **32**, 751–767.

77 S. Mehra, A. Bergerud, D. J. Milliron, E. M. Chan and A. Salleo, *Chem. Mater.*, 2016, **28**, 3454–3461.

78 S. Heitz, Y. Aksu, C. Merschjann and M. Driess, *Chem.–Eur. J.*, 2011, **17**, 3904–3910.

79 G. Schön, *J. Electron Spectrosc. Relat. Phenom.*, 1973, **2**, 75–86.

80 R. Al-Gaashani, S. Radiman, A. R. Daud, N. Tabet and Y. Al-Douri, *Ceram. Int.*, 2013, **39**, 2283–2292.

81 T. Futagami, Y. Aoki, O. Yoda and S. Nagai, *Nucl. Instrum. Methods Phys. Res., Sect. B*, 1994, **88**, 261–266.

82 K. J. Chen, T. H. Fang, F. Y. Hung, L. W. Ji, S. J. Chang, S. J. Young and Y. J. Hsiao, *Appl. Surf. Sci.*, 2008, **254**, 5791–5795.

83 B. E. Sernelius, K.-F. Berggren, Z.-C. Jin, I. Hamberg and C. G. Granqvist, *Phys. Rev. B: Condens. Matter Mater. Phys.*, 1988, **37**, 10244–10248.

84 T. Ratana, P. Amornpitoksuk, T. Ratana and S. Suwanboon, *J. Alloys Compd.*, 2009, **470**, 408–412.

85 V. Etacheri, R. Roshan and V. Kumar, *ACS Appl. Mater. Interfaces*, 2012, **4**, 2717–2725.

86 S. Heitz, Y. Aksu, C. Merschjann and M. Driess, *Chem. Mater.*, 2010, **22**, 1376–1385.

87 A. S. H. Hameed, C. Karthikeyan, S. Sasikumar, V. S. Kumar, S. Kumaresan and G. Ravi, *J. Mater. Chem. B*, 2013, **1**, 5950–5962.

88 X. Peng, J. Xu, H. Zang, B. Wang and Z. Wang, *J. Lumin.*, 2008, **128**, 297–300.

89 M. Suja, S. B. Bashar, M. M. Morshed and J. Liu, *ACS Appl. Mater. Interfaces*, 2015, **7**, 8894–8899.

90 C. Boukaous, B. Benhaoua, A. Telia and S. Ghanem, *Mater. Res. Express*, 2017, **4**, 105024.

91 C. Barrière, G. Alcaraz, O. Margeat, P. Fau, J. B. Quoirin, C. Anceau and B. Chaudret, *J. Mater. Chem.*, 2008, **18**, 3084–3086.

92 M. V. Twigg and M. S. Spencer, *Top. Catal.*, 2003, **22**, 191–203.

93 H. H. Kung, *Catal. Today*, 1992, **11**, 443–453.